Transient critical regime for light near the three-dimensional Anderson transition

Laura A. Cobus, Georg Maret, Alexandre Aubry

Transient critical regime for light near the three-dimensional Anderson transition

Laura A. Cobus,[1, 2, *] Georg Maret,[3] and Alexandre Aubry[1, †]

[1] *Institut Langevin, ESPCI Paris, CNRS, PSL University, 1 rue Jussieu, F-75005 Paris, France*
[2] *Dodd-Walls Centre for Photonic and Quantum Technologies, New Zealand and Department of Physics, University of Auckland, Private Bag 92109, Auckland, New Zealand*
[3] *Fachbereich Physik, Universität Konstanz, D-78457 Konstanz, Germany*

(Dated: September 24, 2021)

We report on anomalous light transport in the strong scattering regime. Using low-coherence interferometry, we measure the reflection matrix of titanium dioxide powders, revealing crucial features of strong optical scattering which can not be observed with transmission measurements: (i) a subdiffusive regime of transport at early times of flight that is a direct consequence of predominant recurrent scattering loops, and (ii) a transition to a conventional, but extremely slow, diffusive regime at long times. These observations support previous predictions that near-field coupling between scatterers prohibits Anderson localization of light in three-dimensional disordered media.

In disordered media, wave transport can be radically affected by strong scattering. Strong scattering generally occurs when the wavelength of propagating waves is comparable to the scale of structure variations in the medium, so that the waves are extremely sensitive to the size and arrangement of the scatterers. For strong enough disorder and scattering strength, Anderson localization can occur, wherein wave diffusion is suppressed exponentially or even halted altogether [1–5]. In particular, three-dimensional (3D) materials are expected to exhibit a phase transition [6] from conventional diffusion to localization, occurring as disorder/energy is varied, or alternately, as the time spent by the waves exploring the sample increases. This behaviour has been observed experimentally for electrons in doped semiconductors [7, 8], vibrations in elastic networks [4, 9], and cold atoms in random potentials [10–12]. Studies of 3D Anderson localization of light, however, remain inconclusive [13–15]. It is possible that none of the materials tested so far scatter light strongly enough to achieve localization [14, 15]; on the other hand, a number of studies have theorized that the onset of localization is prevented by the dipole-dipole interactions between close-packed scatterers [16–19] which are inherent to the vector nature of light [17, 20]. While supported by preliminary evidence [19], this picture has yet to be conclusively experimentally confirmed.

The experimental search of Anderson localization for light is complicated by absorption and nonlinear effects, which become more important the longer the waves spend inside the sample, and which can imitate signatures of localization [14, 21, 22]. Transmission experiments are particularly affected by fluorescence [14], due to the strong incident beams that are required to overcome noise, absorption, and a low probability of transmission near the localization regime. To avoid these issues, we use low-coherence interferometry. Inspired by previous studies in acoustics [23, 24] and seismology [25, 26], our approach enables the measurement of time-dependent Green's functions between points at the surface of a medium which is illuminated by an incoherent light source [27, 28]. This passive type of measurement offers major advantages compared to more conventional methods. First, the reflected wavefield measured via interferometry does not include any signals resulting from spontaneous emission events. Second, a reflection geometry enables the study of: (*i*) interference phenomena that are precursors of Anderson localization, such as coherent backscattering [29, 30] or recurrent scattering [31, 32], and (*ii*) the energy 'halo' in the early-time limit – a temporal regime which is generally inaccessible in transmission.

In this Letter, low-coherence interferometry is applied to some of the strongest scattering samples which exist for light – titanium dioxide (TiO_2) powders. We find that the spatio-temporal spreading of the wave energy exhibits two distinct regimes of transport. At short times of flight t, anomalous diffusion is observed; the spatial extent of the average wave energy, $w^2(t)$, scales as $t^{2/3}$, and the return probability for the energy density scales as t^{-1}. These observations are consistent with the scaling theory of localization [33], suggesting the existence of a critical or localized regime. Yet, after a few hundred femtoseconds, a transition towards conventional diffusion is observed; $w^2(t)$ grows linearly with time, and the temporal decay of the return probability, $t^{-3/2}$, is characteristic of the diffusive regime [34]. Diffusion in this regime is very slow, with a diffusion coefficient of $D \sim 18$ m^2/s. Interestingly, Naraghi and Dogariu [19] predicted a few years ago that such a transition would be caused by strong near-field coupling between scatterers. While transitory behaviour was observed via measurements of return probability [19], these can be subject to absorption or non-linear effects. Here, we report the first experimental observations of the spatio-temporal energy spread throughout this predicted transition. Our results can be described using the aforementioned model, providing strong evidence for the existence of a transition from a critical (pre-localized) to diffuse regime.

* laura.cobus@auckland.ac.nz
† alexandre.aubry@espci.fr

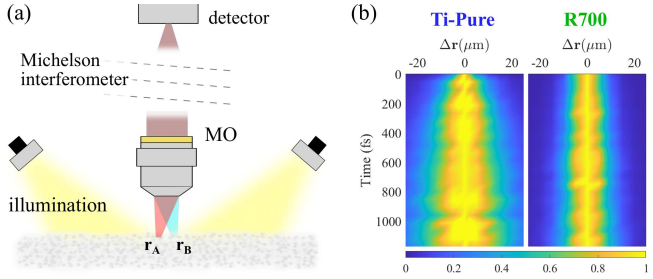

FIG. 1. (a) Low-coherence interferometry measures the cross-correlation between points $\mathbf{r_A}$ and $\mathbf{r_B}$ at the sample surface [27] (MO: microscope objective). (b) Normalized intensity profiles $I(\Delta r, t)/I(0, t)$ are shown for samples Ti-Pure and R700.

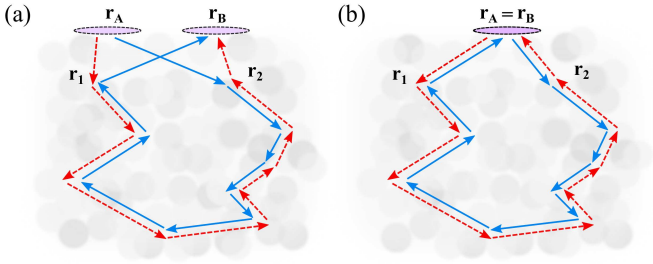

FIG. 2. (a) Coherent backscattering arises from interference between reciprocal paths. Pink oblongs represent the size of virtual sources/receivers at $\mathbf{r}_A$ and $\mathbf{r}_B$. (b) When source and receiver coincide, constructive interference is maximized.

Samples investigated in this work were three different types of TiO_2 powder: a pure anatase phase (Ti-Pure) obtained from Aldrich, and two types of rutile phase powders (R104 and R700) which are commercially available from DuPont as pigments for white paint. Significant Mie scattering resonances can be achieved in these powders, as mean particle size $\langle d \rangle \sim 400 - 800$ nm [35, 36] is on the order of the wavelength of the illuminating light. The powders were compressed into pastille form to decrease the transport mean free path, ℓ^*, and hence increase optical scattering. Scattering strength can be characterized by $k_0\ell^*$, the product of optical wave number k_0 in vacuum and ℓ^*. A value of $k_0\ell^* \sim 1$ indicates very strong scattering, and has been used as an approximate criterion for Anderson localization [33]. Previous measurements have reported $k_0\ell^* \sim 5-6$, $3-4$ and $2-3$ for compressed Ti-Pure, R104 and R700 respectively [37, 38], indicating that light experiences very strong scattering in all three powders. Absorption, on the other hand, is relatively weak, as absorption time τ_a is on the order of 1 ns [37].

We measure the spatio-temporal transport of light in these samples using the low-coherence interferometry apparatus introduced by Badon *et al.* [27, 28] (Fig. 1a). A low-coherence broadband light source ($650 - 850$ nm, radiant flux $\sim 5 \times 10^5$ W.cm^{-2}) illuminates the surface of the sample. The backscattered light is collected by a microscope objective and sent to a Michelson interferometer. A CCD camera measures the output of the interferometer, which is the cross-correlation of the scattered wave-fields in each arm of the interferometer. By translating and tilting the mirrors in each arm, a time-dependent reflection matrix $\mathbf{R}(t)$ can be acquired in a focused basis [28, 39]. This matrix contains the set of impulse responses $R(\mathbf{r}_A, \mathbf{r}_B, t)$ between points at the surface of the scattering sample, $\mathbf{r}_A$ and $\mathbf{r}_B$. Each of these points acts as a virtual source ($\mathbf{r}_A$) or detector ($\mathbf{r}_B$), whose characteristic size is governed by the resolution length δr of the imaging system, here equal to 1.8 μm [39]. The spatio-temporal behaviour of the wave energy density at the surface of the sample is described by the ensemble average of the impulse response intensity: $I(\Delta r, t) \equiv \langle |R(\mathbf{r}_A, \mathbf{r}_B, t)|^2 \rangle$, with $\Delta r = |\mathbf{r}_A - \mathbf{r}_B|$. In practice, this ensemble average is obtained *via* a spatial average over pairs of points $\mathbf{r}_A$ and $\mathbf{r}_B$ separated by the same distance Δr. As discussed in the Supplementary Material [39], our passive imaging method enables the extraction of $I(\Delta r, t)$ from fluorescence and noise contributions that usually pollute active measurements [14, 40].

Figure 1b shows the resulting normalized intensity profile, $I(\Delta r, t)/I(0, t)$, for samples Ti-Pure and R700. The difference between samples is immediately obvious: the stronger scattering in R700 limits the spatial spread of energy compared with Ti-Pure. The spread of $I(\Delta r, t)$ can be quantified by comparing experimental data with theoretical predictions. In the multiple scattering regime, $I(\Delta r, t)$ can be expressed as the sum of two components. The first is an *incoherent* intensity, $I_{\rm inc}$, which is the incoherent average of the intensity of each individual scattering path. The second is a *coherent* intensity correction $I_{\rm coh}$ which takes into account coherent backscattering (CBS) [29, 30], in which waves travelling along pairs of reciprocal paths undergo constructive interference which is not eliminated by the configurational average (Fig. 2).

In real space, the incoherent intensity corresponds to the spatio-temporal spreading of the wave energy density inside the sample – the so-called *diffuse halo*. This spreading can be directly quantified by measuring $w(t)$, the *transverse width* of $I_{\rm inc}(\Delta r, t)$ [41, 42]. In the diffusive regime, $I_{\rm inc}(\Delta r, t)$ can be expressed as follows [34, 39]:

$$I_{\rm inc}(\Delta r, t) = \frac{c e^{-t/\tau_a}}{2\pi^{3/2} w^3(t)} \exp\left[-\frac{\Delta r^2}{w^2(t)}\right], \qquad (1)$$

with

$$w^2(t) = 4 D_B t. \qquad (2)$$

D_B is the Boltzmann diffusion coefficient [34, 41], τ_a is the absorption time, and c the speed of light in the sample. For anomalous wave transport, $w^2(t)$ no longer exhibits a linear increase with time, and $I_{\rm inc}(\Delta r, t)$ could potentially deviate from a Gaussian shape [4, 43].

The CBS effect ($I_{\rm coh}$) manifests as an enhancement in the measured MS intensity at $\Delta r = 0$. The enhancement factor, A, can be defined by the relation $I_{\rm coh}(0, t) = (A - 1) I_{\rm inc}(0, t)$. As Δr increases [Fig.

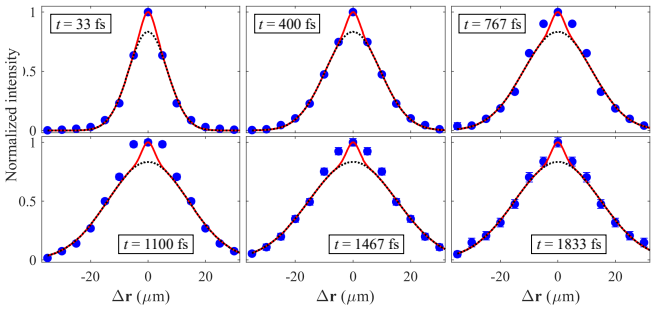

FIG. 3. Normalized intensity profiles $I(\Delta r, t)/I(0, t)$ for sample R104 (solid symbols) at different times (t). Note that experimental error bars are smaller than the symbol size. Red solid lines show theoretical fits with Eq. 3, while black dotted lines represent only the diffuse halo term of Eq. 3.

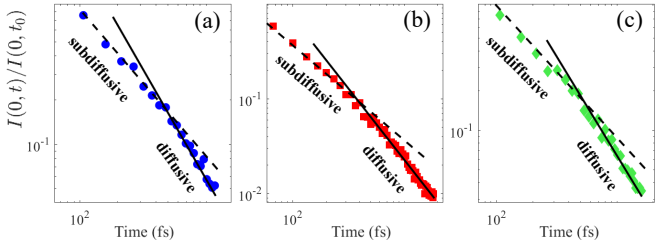

FIG. 4. Return probability $I(0, t)$ normalized by its value at time $t_0 = 53$ fs for (a) Ti-Pure, (b) R104 and (c) R700 (symbols). Lines following $t^{-3/2}$ (solid, diffusive) and t^{-1} (dashed, subdiffusive) are guides to the eye, not fits.

2(b)], the enhancement falls off, giving rise to a peak $F(\Delta r)$ of characteristic width δr [39]. While in **k**-space this CBS peak narrows as time increases [44–46], in real-space its shape is stationary [42, 47, 48]. Ideally, for an experiment with point-like sources and detectors on the medium surface, this CBS peak has the form $I_{\rm coh}(\Delta r, t) \propto [\sin(k\Delta r)/k\Delta r]^2 \exp(-r/\ell_s)$ (ℓ_s is the scattering mean free path) with an enhancement of $A = 2$ [47]. Here, the diffraction limit of our imaging system changes the CBS peak shape to an Airy disk. Low-order aberrations (non-ideal focus and/or astigmatism) can furthermore cause both an increase in CBS peak width and decrease in relative amplitude ($A < 2$) [39].

Altogether, $I(\Delta r, t)$ in the diffusion approximation has the form of a narrow CBS peak on top of a broader time-dependent diffusive halo. The normalized intensity profile can then be written as [39]

$$\frac{I(\Delta r, t)}{I(0, t)} = \frac{1}{A} e^{-\Delta r^2/w^2(t)} + \left(1 - \frac{1}{A}\right) F(\Delta r). \qquad (3)$$

Figure 3 shows $I(\Delta r, t)/I(0, t)$ for sample R104 for six times-of-flight t spanning the entire measurement range. The spatio-temporal spreading of wave energy is clearly exhibited, as is a small and constant CBS enhancement around $\Delta r = 0$. To quantify the energy spread in each sample, the experimental $I(\Delta r, t)$ was compared with the prediction of Eq. 3. Fit parameters were $w^2(t)$ (a free parameter for each time t), and A, which was held constant over time. Note that while the shape of $I(\Delta r, t)$ is only strictly expected to be Gaussian when the diffusion approximation applies, $w^2(t)$ can still give a good quantification of spatio-temporal energy spreading [5], and that in any case, $I(\Delta r, t)$ is well-described by a Gaussian for the entire time range under investigation (Fig. 3). The fitting gives very small values for A which are caused by aberration effects in the experimental setup [39]: $A = 1.12$ for Ti-Pure, $A = 1.2$ for R104, and $A = 1.1$ for R700. Results for $w^2(t)$, however, do not agree with the diffusive prediction of Eq. 2. This implies that our theoretical model must be altered to take into account the extreme strong scattering of our samples.

Compared with conventional diffusion, a key feature of the strong scattering regime ($k\ell^* \sim 1$) is the predominance of recurrent scattering 'loops', *i.e* an increased probability for waves to pass nearby areas that they have previously visited [32, 49, 50]. The time-dependence of this *return probability* can be directly quantified in the reflection geometry by observing the back-scattered intensity at the source location, $I(0, t)$ [Fig. 2(b)]. Figure 4 shows $I(0, t)$ for all three samples. As absorption is negligible for the time range of our measurements, $I(0, t)$ should scale as $t^{-3/2}$ in the diffuse regime (Eq. 1). As the system approaches a transition between diffusion and Anderson localization, the slowing of diffusion can be modeled as a scale-dependent diffusion process [51]. Based on the scaling theory of localization [33], the diffusion coefficient should scale with time as [1, 2, 51]

$$D(t) \simeq \frac{(D_0 \ell^*)^{2/3}}{(6t)^{1/3}}, \qquad (4)$$

with D_0 the diffusion constant in the absence of rescaling. Replacing D_B by the renormalized diffusion coefficient $D(t)$ in Eq. 1 gives the following scaling for the return probability in the localized regime: $I(0, t) \propto t^{-1}$ [52].

Comparison of these theoretical predictions with the experimental data reveals the existence of a transition between two transport regimes at a critical time $\tau_c \sim 425$ fs for Ti-Pure, $\tau_c \sim 400$ fs for R104 and $\tau_c \sim 480$ fs for R700 (Fig. 4). Before τ_c, the return probability scales as t^{-1} which is characteristic of a regime of continuously renormalized diffusion (which falls into the more general category of *subdiffusion*). After the transition ($t > \tau_c$), the return probability scales as $t^{-3/2}$ as expected for diffusion. Naraghi and Dogariu [19] have predicted such a transition, proposing that near-field coupling between scatterers constitutes a 'leak' of energy from propagating paths (e.g. Fig. 2) to evanescent channels. This effect lessens the constructive interference created by recurrent scattering paths, preventing the localization of wave resonances. By modeling recurrent scattering and near-field coupling as competing mechanisms, the critical time can be theoretically expressed as $\tau_c \sim \lambda^2/(3c\ell^*\rho)$ [19, 39], where ρ is the ratio between the near-field and transport cross-sections. Using the values of $\ell^* \sim 0.3$ μm [38]

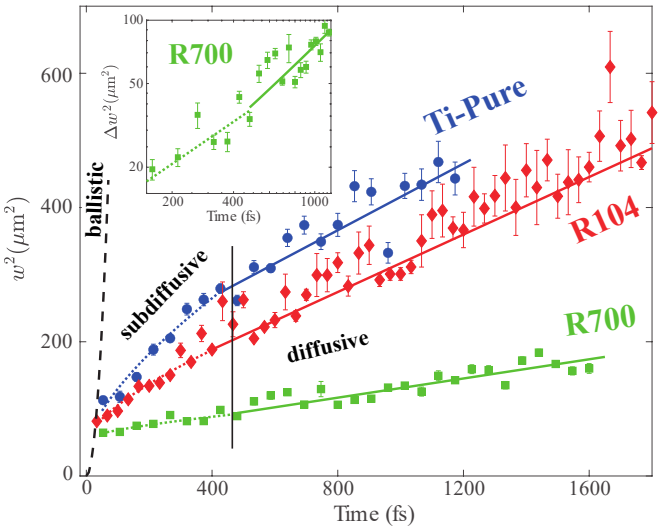

FIG. 5. Transverse width $w^2(t)$ for all three samples (symbols). Error bars represent the uncertainty in $w^2(t)$ due to the (weighted) fitting of $I(\Delta r, t)/I(0, t)$ with Eq. 3. Linear fits to the data (solid lines) give D, for each sample. In the regime of renormalized diffusion ($t < \tau_c$), the data is fit with Eq. 5 (dotted lines). The ballistic light line (dashed black line), indicates the lower limit for $w^2(t)$. Inset: $\Delta\omega^2$ through the subdiffusion-diffusion transition for R700 (log-log scale).

and refractive index $n \sim 2.7$ [37], measured in R700 at $\lambda_0 = 700$ nm, and taking $\tau_c \sim 480$ fs (Fig. 4c), we find $\rho \sim 10^{-2}$. While this small value seems to imply that the energy leak into evanescent channels is negligible, it is for only a few scattering events; in the long-time limit the sheer number of these events results in the extinction of localization and the recovery of diffusion. We note that the observed values of τ_c do not scale with ℓ^*. This is likely due to variation in ρ; although each sample was compressed with the same force, differences in particle size/shape could cause the volume fraction to vary slightly between samples. The differing chemical composition of the samples could also affect the near-field scattering cross-section.

The transition from subdiffusion to diffusion is exhibited more directly in the spatio-temporal spread of wave energy, here quantified via $w(t)$. As shown in Figure 5, $w^2(t)$ increases linearly with time at long times of flight ($t > \tau_c$). This behaviour is predicted by the diffusion approximation, in which $w^2(t) = 4Dt + w_c^2$, where w_c^2 is the lateral extension of the energy halo at critical time τ_c. Linear fits to $w^2(t)$ give a direct measurement of D for each sample: $D = 62 \pm 10$ m^2/s for Ti-Pure, $D = 54 \pm 6$ m^2/s for R104, and $D = 18 \pm 9$ m^2/s for R700. The measured value of D for R700 is in excellent agreement with previous wavelength-dependent measurements performed in transmission [37]: $D \approx 18$ m^2/s for $\lambda = 700$ nm [38]. Other previously reported values are $D \sim 20$ m^2/s for Ti-Pure and $D \sim 18 - 38$ m^2/s for R104 [37], which differ from ours, but were performed for wavelengths at the lowest range of our experimental spectrum. Moreover, the relative values of D that we obtain are logical in light of the differing values of $k\ell^*$ reported for the three samples [37, 38].

For $t < \tau_c$, the time dependence of the return probability (Fig. 4) indicates the renormalization of diffusion. For these times, the behavior of $w^2(t)$ can be predicted by substituting $D(t)$ (Eq. 4) for D_B in Eq. 2, giving

$$w^2(t) = \frac{4}{\sqrt[3]{6}}(D_0 \ell^* t)^{2/3} + w_0^2, \qquad (5)$$

where w_0^2 is the size of the diffuse halo extrapolated to time $t = 0$. Fitting the experimental $w^2(t)$ curves with Eq. 5 confirms the scaling of $w^2(t)$ as $t^{2/3}$ for $t < \tau_c$. The subdiffusion-diffusion transition can be more clearly seen by plotting $\Delta\omega^2 = w^2 - w_0^2$ on a log-log scale – this is shown for R700 in the inset of Fig. 5. Using the value of ℓ^* measured for this sample at $\lambda = 700$ nm [38], an estimate of D_0 can be extracted from the fitting process described by Eq. 5. Remarkably, we find a value of $D_0 \sim 15$ m^2/s, which agrees within error with $D \sim 18 \pm 9$ m^2/s measured from a linear fit of $w^2(t)$ in the diffuse regime (Eq. 2).

A remaining question concerns the transport of light at very early times. The earliest measured point of $w^2(t)$, at $t \sim 50$ fs, is close to the ballistic light line $w(t) = c_0 t$ (Fig. 5). Only super-diffusive – if not ballistic – transport could account for such rapid growth of the diffuse halo. One possible explanation is the existence of ballistic waves propagating at the surface of the scattering sample. This contribution predominates at early times, and may control the dynamics of the diffuse halo in this time range.

In conclusion, we have quantified the spatio-temporal optical energy transport in a strongly scattering regime across a wide range of time scales. Strikingly, we observe a transition between a regime of continuously renormalized diffusion at early times, and a conventional diffusion regime at long times. The observed transition is a manifestation of near-field couplings between scatterers that are inherent to the vector nature of light, and which dominate over recurrent scattering at long times. This effect may explain the elusive 3D Anderson localization of electromagnetic waves. In the long-time diffusive regime, the extremely slow values for the diffusion coefficient D are in agreement with previous experimental measurements performed in transmission [38]. The application of our experimental method to such challenging samples also illuminates the advantages of passive measurements to probe wave phenomena in a strong scattering regime, where non-linear effects, fluorescence, and noise can be increasingly dominant over signals of interest [14, 40]. In the future, a passive measurement of the reflection matrix will constitute a relevant tool to study not only the statistics of the mean intensity, but also the field-field correlations under the framework of random matrix theory [53, 54].

ACKNOWLEDGMENTS

The authors would like to thank Nicolas Lequeux for his help in fabricating the samples, Lukas Schertel for his advice and support, and Sergey Skipetrov and Bart van Tiggelen for fruitful discussions. This project has received funding from the Labex WIFI (Laboratory of Excellence within the French Program Investments for the Future, ANR-10-LABX-24 and ANR-10-IDEX-0001-02 PSL*) and the Agence Nationale de la Recherche (ANR-14-CE26-0032, Research Project LOVE). L. A. C. acknowledges financial support from the European Union's Horizon 2020 research and innovation programme under the Marie Sklodowska-Curie grant agreement No. 744840. A. A. acknowledges financial support from the European Research Council (ERC) under the European Union's Horizon 2020 research and innovation programme (grant agreement No. 819261).

Supplementary Information

This document provides supplementary information to "Transient critical regime for light near the three-dimensional Anderson transition". Here, we provide: (*i*) a description of the experimental setup, (*ii*) a physical interpretation of the setup; (*iii*) the theoretical expression of the mean back-scattered intensity profile, (*iv*) the extraction of this mean intensity profile in the presence of experimental noise, and (*v*) details on the theoretical expression of the critical time.

S1. EXPERIMENTAL SETUP

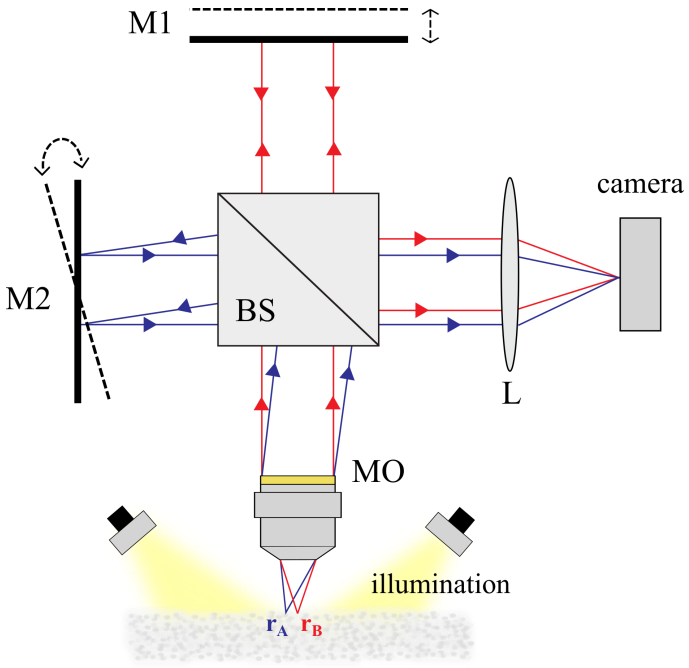

FIG. S1. Experimental setup: a broadband incoherent light source isotropically illuminates a scattering sample. The spatio-temporal correlation of the scattered wave field is extracted by means of a Michelson interferometer and recorded by a camera. MO, microscope objective; BS, beam splitter; M, mirror; L, lens.

The experimental setup employed for the passive measurement of the point-to-point Green's functions at the surface of a scattering sample is sketched in Fig. S1. This measurement has been previously detailed by Badon et al. in Refs [27, 28], and is described here mathematically as a foundation for the following sections.

An incoherent broadband light source ($650 - 850$ nm) isotropically illuminates a scattering sample. The coherence time of the incident wave-field is $\tau_c = 10$ fs [27]. The backscattered wave-field is collected by a microscope objective (NA=0.25) and sent to a Michelson interferometer, which here is used as a spatio-temporal field correlator. The beams coming from the two interference arms are recombined and focused by a lens. A CCD camera conjugated with

the sample surface records the output intensity

$$S_\alpha(\mathbf{r},\mathbf{r}+\Delta\mathbf{r},t)=\int_0^T |e^{i\alpha}\psi(\mathbf{r},t+\tau)+\psi(\mathbf{r}+\Delta\mathbf{r},\tau)|^2\mathrm{d}\tau, \tag{S1}$$

where τ is the absolute time, $\mathbf{r}$ the position vector on the CCD screen, $\psi(\mathbf{r},\tau)$ the scattered wave field associated with the first interference arm, T the integration time of the camera, and α an additional phase term controlled with a piezoelectric actuator placed on mirror M_1. The tilt of mirror M_2 allows a displacement $\Delta\mathbf{r}$ of the associated wave-field at the camera. The motorized translation of mirror M_1 induces a time delay $t=\delta/c$ between the two interferometer arms, with δ the optical path difference (OPD) and c_0 the light celerity in vacuum. The interference term is extracted from the four intensity patterns Eq. S1) recorded at $\alpha=0$, $\pi/2$, $3\pi/2$ and π ("four phase method" [28]). On each pixel of the camera, we thus measure the cross-correlation $C(\mathbf{r}_A,\mathbf{r}_B,t)$ between scattered wave-fields, $\psi_c(\mathbf{r}_A,\tau)$ and $\psi_c(\mathbf{r}_B,\tau)$, associated with each arm of the interferometer:

$$C_T(\mathbf{r}_A,\mathbf{r}_B,t)=\frac{1}{T}\int_0^T \psi(\mathbf{r}_A,t+\tau)\psi^*(\mathbf{r}_B,\tau)\mathrm{d}\tau, \tag{S2}$$

where τ is the absolute time, $\mathbf{r}_A$ and $\mathbf{r}_B$ are the points in the focal plane of the microscope objective that are conjugated with the same pixel on the camera, and $\Delta\mathbf{r}=\mathbf{r}_B-\mathbf{r}_A$. In an ideal case (fully incoherent incident light and NA=1), the correlation function $C(\mathbf{r}_A,\mathbf{r}_B,t)$ would converge towards the Green's function between points $\mathbf{r}_A$ and $\mathbf{r}_B$ for an infinite integration time [27, 28]. In practice, the limited numerical aperture of our experimental device induces aberrations. This implies that our measurement scheme does not give direct access to the true Green's function between points $\mathbf{r}_A$ and $\mathbf{r}_B$; rather, we measure the response between a virtual source at point $\mathbf{r}_A$ and a virtual detector at point $\mathbf{r}_B$. In the following, we will see the consequences that result from the finite spatial extent of our virtual source/detector.

S2. PHYSICAL INTERPRETATION OF OUR PASSIVE IMAGING METHOD

The scattered wave-field ψ_c measured by the camera is now investigated in the temporal Fourier domain. Using the Rayleigh-Sommerfeld integral, ψ_c can be expressed as [55]

$$\psi_c(\mathbf{r_A},\omega)=jk\int_S d\mathbf{r}\ H(\mathbf{r}-\mathbf{r}_A,\omega)\psi_s(\mathbf{r},\omega), \tag{S3}$$

where S is the surface of the scattering medium, ω is frequency, $k=\omega/c$ is the optical wave number, c is optical wave-speed, $\psi_s(\mathbf{r},\omega)$ is the optical wave-field at the surface of the sample, and $H(\mathbf{r}-\mathbf{r}_A,\omega)$ is the spatial impulse response between the sample and the camera. In the following, given the limited bandwidth of the light source ($\Delta\omega/\omega\sim 30\%$), the impulse response H will be taken as independent of frequency ω. The time-derivative of the mutual coherence function of this wave-field can be expressed as

$$\begin{aligned} R(\mathbf{r}_A,\mathbf{r}_B,\omega) &\equiv j\omega\langle\psi_c(\mathbf{r_A},\omega)\psi_c^*(\mathbf{r_B},\omega)\rangle_t \\ &= j\omega k^2\int_S d\mathbf{r}_1\int_S d\mathbf{r_2}\ H(\mathbf{r}_1-\mathbf{r}_A)H^*(\mathbf{r}_2-\mathbf{r}_B)\langle\psi_s(\mathbf{r}_1,\omega)\psi_s^*(\mathbf{r_2},\omega)\rangle, \end{aligned}$$

where the symbol $\langle\cdots\rangle$ denotes an ensemble average. For an ambient wave field $\psi_s(\mathbf{r},\omega)$ equipartitioned in energy in phase space, the fluctuation-dissipation theorem implies that the time-derivative of the mutual coherence function $\langle\psi_s(\mathbf{r}_1,\omega)\psi_s^*(\mathbf{r}_2,\omega)\rangle$ converges towards the imaginary part of the Green's function between $\mathbf{r}_1$ and $\mathbf{r}_2$ [56]:

$$j\omega\langle\psi_s(\mathbf{r}_1,\omega)\psi_s^*(\mathbf{r}_2,\omega)\rangle=\mathrm{Im}G(\mathbf{r}_1,\mathbf{r}_2,\omega)=[G(\mathbf{r}_1,\mathbf{r}_2,\omega)-G^*(\mathbf{r}_1,\mathbf{r}_2,\omega)]. \tag{S4}$$

Here, $G(\mathbf{r}_1,\mathbf{r}_2,\omega)$ and $G^*(\mathbf{r}_1,\mathbf{r}_2,\omega)$ stand for the causal (retarded) and anti-causal(advanced) parts of the Green's function, respectively. In our measurement, only the causal part ($t>0$) of the correlation signal $C_T(\mathbf{r}_A,\mathbf{r}_B,t>0)$ is recorded. Hence, $\mathrm{Im}G(\mathbf{r}_1,\mathbf{r}_2,\omega)$ can be replaced by the retarded Green's function in Eq. S4, such that

$$R(\mathbf{r_A},\mathbf{r_B},\omega)=k^2\int_S d\mathbf{r}_1\int_S d\mathbf{r}_2 H(\mathbf{r}_1-\mathbf{r}_A)G(\mathbf{r}_1,\mathbf{r}_2,\omega)H^*(\mathbf{r}_2-\mathbf{r}_B). \tag{S5}$$

This equation can be given the following physical interpretation by reading the integrands from left to right: $H(\mathbf{r}_1-\mathbf{r_A})$ describes the amplitude distribution at point $\mathbf{r}_1$ of an incident wave-field generated by a virtual source located at $\mathbf{r}_A$, $G(\mathbf{r}_1,\mathbf{r}_2,\omega)$ describes wave propagation in the sample from $\mathbf{r}_1$ to $\mathbf{r}_2$ where the first and last scattering events occur, and $H^*(\mathbf{r}_2-\mathbf{r_B})$ describes the propagation between the last scattering event and the virtual detector at $\mathbf{r_B}$. The covariance matrix $\mathbf{R}(\omega)=[R(\mathbf{r_A},\mathbf{r_B},\omega)]$ can thus be seen as the reflection matrix of the scattering medium measured in real space.

S3. THEORETICAL DESCRIPTION OF THE MEAN INTENSITY PROFILE

In the present work, we are interested in the spatio-temporal evolution of the mean backscattered intensity. A theoretical prediction for this quantity can be derived by considering the ensemble averaged intensity of the time-dependent mutual coherence function:

$$I(\mathbf{r}_A, \mathbf{r}_B, t) = \langle |R(\mathbf{r_A}, \mathbf{r_B}, t)|^2 \rangle. \tag{S6}$$

To express $I(\mathbf{r}_A, \mathbf{r}_B, t)$, we will first consider its temporal frequency counterpart, $I(\mathbf{r}_A, \mathbf{r}_B, \Omega)$:

$$I(\mathbf{r}_A, \mathbf{r}_B, \Omega) = \int dt I(\mathbf{r}_A, \mathbf{r}_B, t) e^{-i\Omega t}. \tag{S7}$$

Using Eq. S6, $I(\mathbf{r}_A, \mathbf{r}_B, \Omega)$ can be rewritten as

$$I(\mathbf{r}_A, \mathbf{r}_B, \Omega) = \langle R(\mathbf{r}_A, \mathbf{r}_B, \omega) R^*(\mathbf{r}_A, \mathbf{r}_B, \omega - \Omega) \rangle_\omega. \tag{S8}$$

Injecting Eq. S5 into Eq. S8 gives

$$\begin{aligned} I(\mathbf{r}_A, \mathbf{r}_B, \Omega) =& k^4 \int_S d\mathbf{r}_1 \int_S d\mathbf{r}_2 \int_S d\mathbf{r}'_1 \int_S d\mathbf{r}'_2 H(\mathbf{r}_1 - \mathbf{r}_A) H^*(\mathbf{r}'_1 - \mathbf{r}_A) \\ & \times \langle G(\mathbf{r}_1, \mathbf{r}_2, \omega) G^*(\mathbf{r}'_1, \mathbf{r}'_2, \omega - \Omega) \rangle_\omega H^*(\mathbf{r}_2 - \mathbf{r}_B) H(\mathbf{r}'_2 - \mathbf{r}_B). \end{aligned} \tag{S9}$$

In the weak scattering regime ($k\ell^* >> 1$), most contributions to the correlation function of the Green's function at the surface of the scattering medium, $\langle G(\mathbf{r}_1, \mathbf{r}_2, \omega) G^*(\mathbf{r}'_1, \mathbf{r}'_2, \omega - \Omega) \rangle_\omega$, will cancel out in the above ensemble average. The only contributions to survive this average are those for which the wave and its complex conjugate experience identical paths. This condition is achieved if the wave and the complex conjugate visit the same scatterers either in the same order (ladder diagrams), or in reversed order (maximally crossed diagrams). The correlation function can thus be decomposed into two terms [57]:

$$\langle G(\mathbf{r}_1, \mathbf{r}_2, \omega) G^*(\mathbf{r}'_1, \mathbf{r}'_2, \omega - \Omega) \rangle_\omega = \frac{c}{k^4} P(\mathbf{r}_1, \mathbf{r}_2, \Omega) \left[\delta(\mathbf{r}_1 - \mathbf{r}'_1) \delta(\mathbf{r}_2 - \mathbf{r}'_2) + \delta(\mathbf{r}_1 - \mathbf{r}'_2) \delta(\mathbf{r}'_1 - \mathbf{r}_2) \right], \tag{S10}$$

where $P(\mathbf{r}_1, \mathbf{r}_2, \Omega)$ is an energy density. Physically, $P(\mathbf{r}_1, \mathbf{r}_2, \Omega)$ is the Fourier transform of $P(\mathbf{r}_1, \mathbf{r}_2, t)$ – the probability to find a pulse at point $\mathbf{r}$ and time t, after emission of a short pulse at point $\mathbf{r}'$. The first term of Eq. S10 describes the self-interference of the wave associated with each possible scattering path between $\mathbf{r}_1$ and $\mathbf{r}_2$. The second describes the constructive interference between reciprocal scattering paths between the same points.

Injecting Eq. S10 into Eq. S9 leads to a decomposition of the mean back-scattered intensity as the sum of an incoherent (I_{inc}) and a coherent (I_{coh}) component. In the temporal regime, this can be expressed as

$$I(\mathbf{r}_A, \mathbf{r}_B, t) = I_{\text{inc}}(\mathbf{r}_A, \mathbf{r}_B, t) + I_{\text{coh}}(\mathbf{r}_A, \mathbf{r}_B, t). \tag{S11}$$

The incoherent intensity I_{inc} accounts for the self interference of waves propagating along the same scattering paths,

$$I_{\text{inc}}(\mathbf{r}_A, \mathbf{r}_B, t) = c \int_S d\mathbf{r}_1 \int_S d\mathbf{r}_2 \; |H(\mathbf{r}_1 - \mathbf{r}_A)|^2 P(\mathbf{r}_2, \mathbf{r}_1, t) |H(\mathbf{r}_2 - \mathbf{r}_B)|^2, \tag{S12}$$

while the coherent intensity I_{coh} is associated with the interference of waves propagating along reciprocal scattering paths,

$$I_{\text{coh}}(\mathbf{r}_A, \mathbf{r}_B, t) = c \int_S d\mathbf{r}_1 \int_S d\mathbf{r}_2 H(\mathbf{r}_1 - \mathbf{r}_A) H(\mathbf{r}_1 - \mathbf{r}_B) P(\mathbf{r}_2, \mathbf{r}_1, t) H^*(\mathbf{r}_2 - \mathbf{r}_A) H^*(\mathbf{r}_2 - \mathbf{r}_B). \tag{S13}$$

This term accounts for the so-called coherent backscattering phenomenon. To simplify the preceeding expressions, the medium can be assumed to be statistically homogeneous such that P is invariant by translation: $P(\mathbf{r}_2, \mathbf{r}_1, t) = P(\mathbf{r}_2 - \mathbf{r}_1, t)$. Then, the incoherent intensity (Eq. S12) can be simplified to:

$$I_{\text{inc}}(\Delta r, t) = c \left[|H|^2 \overset{\Delta \mathbf{r}}{\circledast} |H|^2 \overset{\Delta \mathbf{r}}{\circledast} P(\Delta \mathbf{r}, t) \right], \tag{S14}$$

where $\Delta \mathbf{r} = \mathbf{r}_B - \mathbf{r}_A$ is the relative position between the virtual source and detector and the symbol $\overset{\Delta \mathbf{r}}{\circledast}$ stands for the correlation product over $\Delta \mathbf{r}$.

In the weak disorder regime ($k\ell^* >> 1$), $P(\Delta\mathbf{r}, t)$ is the solution to the diffusion equation, in which diffusivity $\mathcal{D}$ is constant and corresponds to the Boltzmann diffusion coefficient $\mathcal{D} = D_B = v_E\ell^*/3$, where v_E is the energy transport velocity. In this regime [34],

$$P(\Delta\mathbf{r}, t) = \frac{1}{\pi^{3/2}w^3(t)} \exp\left[-\frac{|\Delta\mathbf{r}|^2}{w^2(t)}\right] \tag{S15}$$

where the spatial extent of this energy 'halo' $w^2(t)$ is

$$w^2(t) = 4D_B t. \tag{S16}$$

For stronger disorder ($k\ell^* \sim 1$), an increase in the probability of recurrent scattering paths can cause a renormalization (decrease) of the diffusion coefficient. The self-consistent theory of localization predicts that, in 3D, D scales as [1, 2]:

$$D \approx D_0\ell^* \left(\frac{1}{\xi} + \frac{1}{L} + \frac{1}{L_A}\right), \tag{S17}$$

where D_0 is the diffusion coefficient before rescaling, ξ is the correlation length defining the spatial coherence of a wavefield in the delocalized regime, L is the system size, and L_A is the absorption length. In reflection, the effective system size L can be said to be the spatial extent of the wave spread, $L(t) = \sqrt{6D(t)t}$ [51]. Thus, before reaching localization ($L << \xi$) and if absorption is negligible ($L << L_a$), Eq. S17 leads to the following time-dependence for the diffusion coefficient:

$$D(t) \simeq \frac{(D_0\ell^*)^{2/3}}{(6t)^{1/3}}. \tag{S18}$$

Replacing D_B by $D(t)$ in Eq. S16 allows an estimate of the scaling of $w^2(t)$ in the presence of strong scattering:

$$w^2(t) \approx \frac{4}{\sqrt[3]{6}}(D_0\ell^* t)^{2/3} \tag{S19}$$

Before reaching a localized regime, the growth of the diffuse halo is thus sub-diffusive.

As soon as $w^2(t)$ is much larger than the spatial extent δr^2 of $|H|^2$ ($w^2(t) >> \delta r^2$), the incoherent intensity (Eq. S14) is a reliable estimator of $P(\Delta\mathbf{r}, t)$:

$$I_{\text{inc}}(\Delta\mathbf{r}, t) \underset{\delta r^2 << w^2(t)}{\sim} cP(\Delta\mathbf{r}, t). \tag{S20}$$

Under the same condition , $P(\mathbf{r}_2 - \mathbf{r}_1, t)$ can be replaced by $P(\mathbf{0}, t)$ in the integrand of Eq. S13. The expression of I_{coh} then simplifies into:

$$I_{\text{coh}}(\Delta\mathbf{r}, t) \underset{\delta r^2 << w^2(t)}{\sim} cP(\mathbf{0}, t) \times |H \overset{\Delta\mathbf{r}}{*} H|^2(\Delta\mathbf{r}), \tag{S21}$$

where the symbol $\overset{\Delta\mathbf{r}}{*}$ stands for a convolution product over $\Delta\mathbf{r}$. In our experimental configuration where $\delta r^2 = 3.2\ \mu\text{m}^2$, this condition is already reached at the earliest measured times of flight; thus, the shape of the CBS peak is governed by the coherent PSF $|H \overset{\Delta\mathbf{r}}{*} H|^2(\Delta\mathbf{r})$ for all times.

Using Eqs. S14 and S21, a theoretical expression for the coherent backscattering enhancement A can be derived:

$$A = 1 + \frac{I_{\text{coh}}(\Delta r = 0)}{I_{\text{inc}}(\Delta r = 0)} = 1 + \frac{|H \overset{\Delta\mathbf{r}}{*} H|^2(\Delta r = 0)}{|H|^2 \overset{\Delta\mathbf{r}}{\circledast} |H|^2(\Delta r = 0)}. \tag{S22}$$

The shape of the CBS peak is given by the function

$$F(\Delta r) = \frac{|H \overset{\Delta\mathbf{r}}{*} H|^2(\Delta r)}{|H \overset{\Delta\mathbf{r}}{*} H|^2(\Delta r = 0)}. \tag{S23}$$

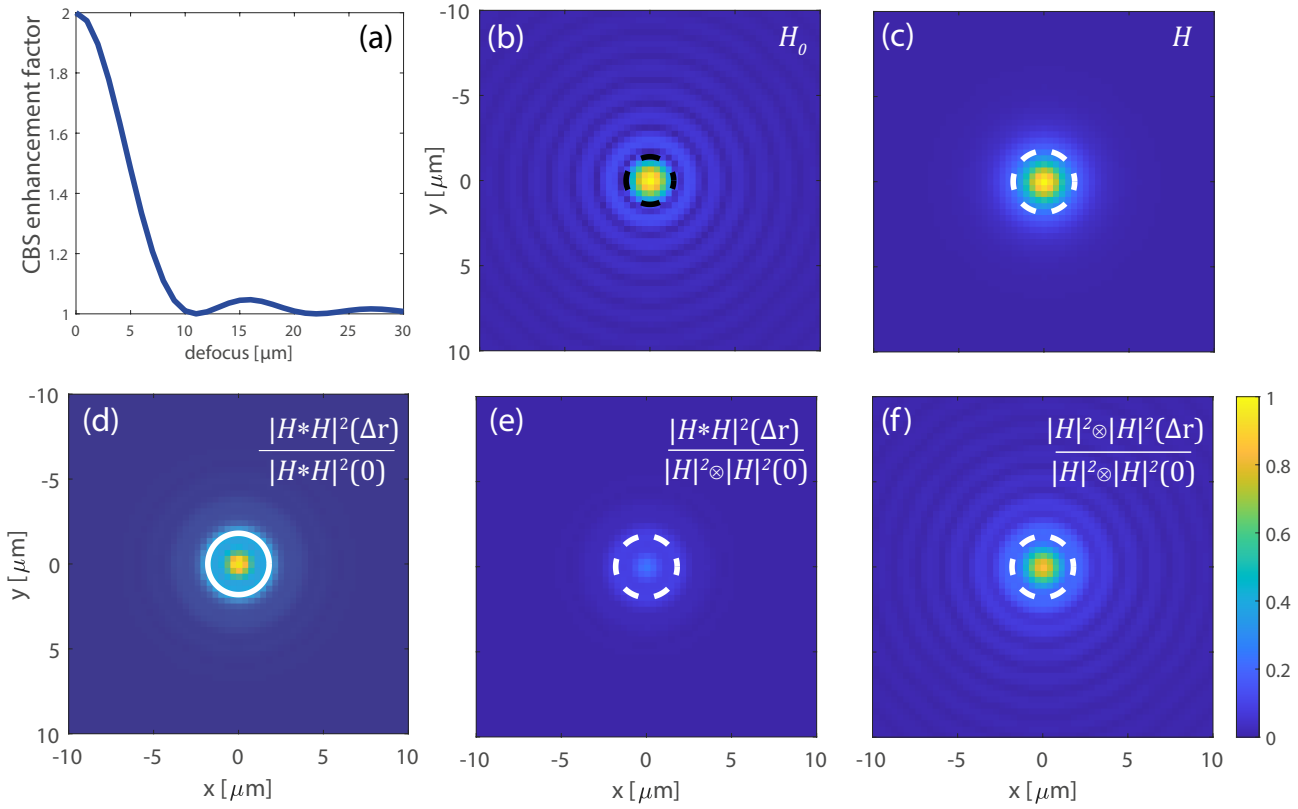

FIG. S2. (a) Evolution of the CBS enhancement factor A as a function of defocus. (b) Diffraction-limited PSF $H_0(\mathbf{r})$. The dashed black circle accounts for the diffraction limited focal spot of radius $\delta r \sim \lambda/(2NA) \sim 1.4$ μm. (c) PSF $H(\mathbf{r})$ for a defocus $z = 7$ μm. (d,e) Corresponding CBS peak $|H \overset{\Delta\mathbf{r}}{*} H|^2(\Delta\mathbf{r})$ normalized by its maximum (c) and the incoherent PSF $|H|^2 \overset{\Delta\mathbf{r}}{\circledast} |H|^2$ at Δr=0. (f) Corresponding incoherent PSF $|H|^2 \overset{\Delta\mathbf{r}}{\circledast} |H|^2(\Delta\mathbf{r})$. In panels (c)-(e), the white dashed circle accounts for the defocused focal spot of radius $\delta r \sim zNA/\sqrt{1-NA^2} \sim 1.8$ μm.

In the absence of aberrations, the PSF is only limited by diffraction: $H \equiv H_0$, with $H_0 = \sqrt{2}J_1(kNA\Delta r)/(kNA\Delta r)$ (Fig. S2(b)). In this ideal case, the CBS enhancement A is equal to 2 since $|H_0|^2 \overset{\Delta\mathbf{r}}{\circledast} |H_0|^2(\Delta r = 0) \equiv |H_0 \overset{\Delta\mathbf{r}}{*} H_0|^2(\Delta r = 0)$. The CBS peak then coincides with the Airy disk: $F(\Delta r) = |H_0(\Delta r)|^2$.

In the real world, any imaging system suffers from aberrations. Relying on a simple Fourier optics model [58], Fig. S2(a) shows, for instance, the effect of a defocus on the CBS enhancement. The enhancement factor A falls off rapidly with the defocus distance d and cancels for $d = nz_R/2$, where n is a positive integer and $z_R = 2\lambda/NA^2 \sim 22$ μm is the Rayleigh range or depth-of-field. The weak CBS enhancement ($A \sim 0.1 - 0.2$) found in our experiments would correspond to a defocus of $d \sim 7$ μm. The corresponding PSF H, the associated CBS peak $F(\Delta\mathbf{r})$ and the incoherent PSF $|H|^2 \overset{\Delta\mathbf{r}}{\circledast} |H|^2(\Delta\mathbf{r})$ are displayed for this value of defocus in Fig. S2(c), (d,e) and (f), respectively. This figure illustrates the drastic effect of defocus on the CBS peak with respect to the incoherent PSF. The spatial extent δr of each quantity is roughly equal to the transverse resolution in presence of a defocus z: $\delta r \sim zNA/\sqrt{1-NA^2} \sim 1.8$ μm [58]. Higher-order aberrations such as astigmatism could also contribute to the weak value of CBS enhancement observed in our experiments.

S4. MEASUREMENT OF $I(\Delta\mathbf{r}, t)$ IN THE PRESENCE OF NOISE

Because of the incoherence of the illumination, the ensemble average of $C(\mathbf{r_A}, \mathbf{r_B}, t)$ should be theoretically achieved by integrating the interferometric signal over an infinite integration time T (Eq.S2):

$$\lim_{T\to+\infty} C_T(\mathbf{r_A}, \mathbf{r_B}, t) = R(\mathbf{r_A}, \mathbf{r_B}, t). \tag{S24}$$

In practice, T is finite and the convergence of C_T towards its ensemble average cannot be completely assured. The situation is made worse by the fact that, for large Δr and time lapse t, the signal of interest can be very weak, and undesirable noisy contributions such as shot noise and fluorescence may dominate.

To evaluate the convergence of C_T towards R, one can consider the intensity profile $I_T(\Delta r, t)$ averaged over pairs of points $\mathbf{r}_A$ and $\mathbf{r}_B$ separated by the same distance Δr:

$$I_T(\Delta r, t) = \langle |C_T(\mathbf{r}_A, \mathbf{r}_B, t)|^2 \rangle_{\{(\mathbf{r}_A, \mathbf{r}_B) \,|\, |\mathbf{r}_A - \mathbf{r}_B| = \Delta r\}}. \tag{S25}$$

Here, we have assumed that disorder is statistically homogeneous. The evolution of $I_T(\Delta r)$ as a function of T is given by [28]

$$I_T\left(\Delta r, t\right) = I\left(\Delta r, t\right) + \frac{\delta t}{T} \langle |N(\Delta r, t)|^2 \rangle_{\{(\mathbf{r}_A, \mathbf{r}_B) \,|\, |\mathbf{r}_A - \mathbf{r}_B| = \Delta r\}}, \tag{S26}$$

where

$$I(\Delta r, t) = \langle |R(\mathbf{r_A}, \mathbf{r_B}, t)|^2 \rangle_{\{(\mathbf{r}_A, \mathbf{r}_B, t) \,|\, |\mathbf{r}_A - \mathbf{r}_B| = \Delta r\}} \tag{S27}$$

is the mean intensity profile for an infinite integration time. $N(\Delta r, t)$ represents the contribution of incoherent noise whose coherence time is governed by the source bandwidth and thus scales as $\delta t/T$. The noise contribution corresponds to the part of the wave-field whose cross-correlation function vanishes with the average over T in Eq. S26. Shot noise and fluorescence signals that result from spontaneous emission events thus emerge along this noise contribution.

Figure S3 shows representative results for $I_T\left(\Delta r, t\right)$ as a function of T (solid symbols). Results for several values of Δr are shown for times of flight (a) $t = 0$ fs and (b) $t = 1200$ fs. For small integration times, $I_T\left(\Delta r, t\right)$ decreases as $1/T$, as expected for noise. At large T, and for small values of Δr and t, $I_T\left(\Delta r, t\right)$ plateaus at the value of $I\left(\Delta r, t\right)$. In previous works [27, 28], 'by eye' examination of such convergence curves was performed to estimate whether or not $I_T\left(\Delta r, t\right)$ had converged satisfactorily towards $I\left(\Delta r, t\right)$. Points for which the convergence curve is well above the noise level (black dotted lines in Fig. S3) were deemed acceptable. This noise level was then taken to be the intensity measured at the maximum Δr and t of the scan, assumed constant over space and time, and subtracted from $I_T\left(\Delta r, t\right)$ to obtain $I_T\left(\Delta r, t\right)$. For accurate measurements at much longer times of flight, however, this method is no longer viable. Figure S3 shows an example of convergence curves measured for sample R104. Even with a very large integration time, $I_T\left(\Delta r, t\right)$ does not converge to a constant value for some values of Δr at the relatively short time of $t = 33$ fs [Fig. S3(a)], or for any spatial position at the later time $t = 1000$ fs [Fig. S3(b)]. It is clear that another method of extracting $I\left(\Delta r, t\right)$ from noise is required. To this end, we introduce a simple yet powerful alternate method. We fit the experimental $I_T\left(\Delta r, t\right)$ versus $1/T$ with a straight line; the slope gives the noise level while the y-offset gives $I\left(\Delta r, t\right)$ according to Eq. S26. This fit is a weighted fit, with experimental uncertainty $\sigma(T)$ taken to be the error in the mean over pixels $\mathbf{r}$ in the calculation of $I_T(\Delta r, t)$ (Eq. S27), for each integration time T. In Fig. S3, representative results for this fitting procedure are shown (solid lines). For all positions and times, the data can be very well fit with the form of Eq. (S26). The uncertainty in $I\left(\Delta r, t\right)$ is given by [59]

$$\sigma_I = \sqrt{\frac{1}{\Delta} \sum_T \frac{(1/T)^2}{\sigma(T)^2}}, \tag{S28}$$

where

$$\Delta = \sum_T \frac{1}{\sigma(T)^2} \sum_T \frac{(1/T)^2}{\sigma^2(T)} - \left(\sum_T \frac{(1/T)^2}{\sigma^2(T)} \right)^2. \tag{S29}$$

Figure S4 shows normalized intensity profiles for sample R104, calculated using (a) the noise subtraction method from previous studies [27, 28], and (b) the $I_T\left(\Delta r, t\right)$ fitting approach introduced in this work. In Fig. S4(a), the data give the impression that energy is spreading much more slowly than it appears in Fig. S4(b). This spread even seems to stop at long times of flight – a feature that could be wrongly attributed to Anderson localization [14, 40]. Such contributions from incoherent noise can thus hamper accurate observations of the diffuse halo, as had already been observed for fluorescent noise in a transmission geometry [14, 40]. The 'false' plateau reached by the diffuse halo in Fig. S4(a) occurs because the noise subtraction method overestimates the noise level at the largest Δr and t in the measured range, for a (finite) number of averages. Subtracting this estimated noise level then results in narrower intensity profiles at long times. In contrast, the $I_T\left(\Delta r, t\right)$ fitting approach uses the data gathered over a finite range of Δr and t to properly estimate the noise level at each point (Δr,t).

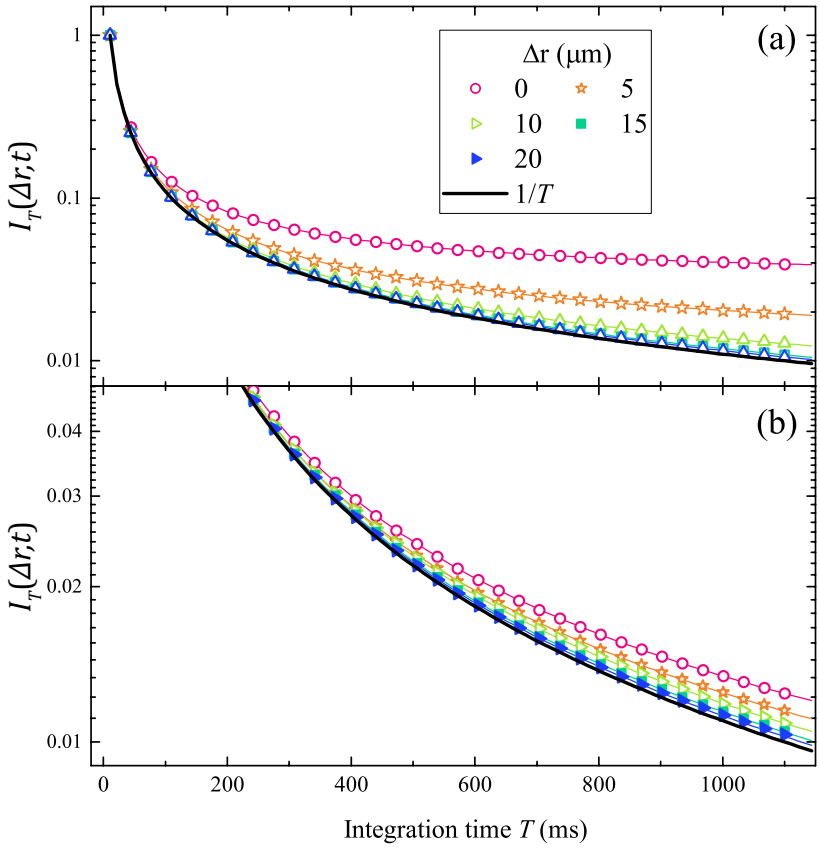

FIG. S3. Average correlation function (solid symbols) as a function of integration time (number of averages). Data shown is for R104 for several representative values of Δr, at times of flight (a) $t = 33$ fs and (b) 1000 fs. Corresponding fits [Eq. (S26)] are shown as solid lines. In both (a) and (b) $1/T$ is represented by a thick black solid line. For clarity, experimental uncertainties are not shown.

S5. THEORETICAL EXPRESSION OF THE CRITICAL TIME

As shown by Naraghi and Dogariu [19], the phase transition between the sub-diffusive and diffusive regime takes place when the probabilities of recurrent scattering and near-field leaking become comparable. The recurrent scattering probability, $p_\times$, is determined by the ratio between the trajectory volume and the volume the light explores inside the multiple scattering medium [57]. In a reflection geometry, $p_\times$ is stationary and given by [19],

$$p_\times \sim \frac{\lambda^2}{2\ell^{*2}}. \tag{S30}$$

Let us now investigate the near-field coupling between scatterers that may inhibit scattering loops inside the medium. At high concentration of particles, the energy can leak out of the diffusive channels because of the near-field interactions between scatterers located at less than a wavelength apart. The corresponding leaking probability, p_{leak}, along a wave trajectory of length s is given by [19]

$$p_{leak} \sim \frac{3}{2} n_0 \sigma_{NF} s, \tag{S31}$$

where n_0 is the particle concentration and σ_{NF} is the near-field cross-section of an individual scatterer. Setting $p_\times$ (Eq. S30) and p_{leak} (Eq. S31) to be equal, a critical path length s_c can be derived:

$$s_c \sim \frac{\lambda^2}{3\ell^{*2} n_0 \sigma_{NF}}. \tag{S32}$$

This last equation leads to the final expression of the critical time $\tau_c = s_c/c$ provided in the accompanying Letter:

$$\tau_c \sim \frac{\lambda^2}{3c\ell^*} \frac{\sigma_t}{\sigma_{NF}}, \tag{S33}$$

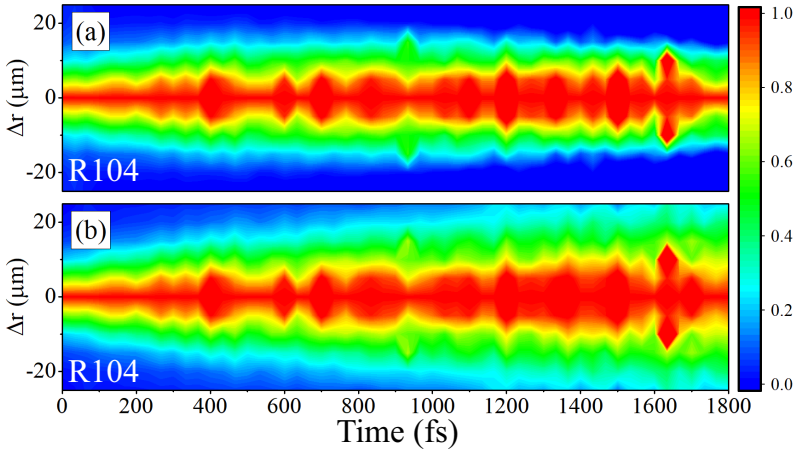

FIG. S4. Comparison of intensity extraction approaches for sample R104. (a,b) Diffuse halos for R104; in (a), the noise subtraction method overestimates the noise level, resulting in a narrower halo at long times than does the convergence method shown in (b).

where $\sigma_t \sim 1/(n_0\ell^*)$ is the transport cross-section of an individual scatterer.

[1] P. W. Anderson, Absence of Diffusion in Certain Random Lattices, Phys. Rev. **109**, 1492 (1958).
[2] S. John, Electromagnetic Absorption in a Disordered Medium near a Photon Mobility Edge, Phys. Rev. Lett. **53**, 2169 (1984).
[3] S. John, Localization of Light, Phys. Today **44**, 32 (1991).
[4] H. Hu, A. Strybulevych, J. H. Page, S. E. Skipetrov, and B. A. van Tiggelen, Localization of ultrasound in a three-dimensional elastic network, Nat. Phys. **4**, 945 (2008).
[5] L. A. Cobus, W. K. Hildebrand, S. E. Skipetrov, B. A. van Tiggelen, and J. H. Page, Transverse confinement of ultrasound through the Anderson transition in three-dimensional mesoglasses, Phys. Rev. B. **98**, 214201 (2018).
[6] F. Evers and A. D. Mirlin, Anderson transitions, Rev. Mod. Phys. **80**, 1355 (2008).
[7] T. Rosenbaum, K. Andres, G. Thomas, and R. Bhatt, Sharp metal-insulator transition in a random solid, Phys. Rev. Lett. **45** (1980).
[8] P. A. Lee and T. V. Ramakrishnan, Disordered electronic systems, Rev. Mod. Phys. **57**, 287 (1985).
[9] L. A. Cobus, A. Aubry, S. E. Skipetrov, B. A. van Tiggelen, A. Derode, and J. H. Page, Anderson mobility gap probed by dynamic coherent backscattering, Phys. Rev. Lett. **116**, 193901 (2016).
[10] J. Chabé, G. Lemarié, B. Gréemaud, D. Delande, P. Szriftgiser, and J. Garreau, Experimental experimental observation of the Anderson metal–insulator transition with atomic matter waves, Phys. Rev. Lett. **101**, 255702 (2008).
[11] S. S. Kondov, W. R. McGehee, J. J. Zirbel, and B. DeMarco, Three-dimensional Anderson localization of ultracold matter, Science **334**, 66 (2011).
[12] F. Jendrzejewski, A. Bernard, K. Müller, P. Cheinet, V. Josse, M. Piraud, L. Pezzé, L. Sanchez-Palencia, A. Aspect, and P. Bouyer, Three-dimensional localization of ultracold atoms in an optical disordered potential, Nat. Phys. **8**, 398 (2012).
[13] T. van der Beek, P. Barthelemy, P. M. Johnson, D. S. Wiersma, and A. Lagendijk, Light transport through disordered layers of dense gallium arsenide submicron particles, Phys. Rev. B. **85**, 1 (2012).
[14] T. Sperling, L. Schertel, M. Ackermann, G. J. Aubry, C. M. Aegerter, and G. Maret, Can 3D light localization be reached in 'white paint'?, New J. Phys. **18**, 13039 (2016).
[15] S. E. Skipetrov and J. H. Page, Red light for Anderson localization, New J. Phys. **18**, 21001 (2016).
[16] S. John, Phys. Today **45**, 122 (1992).
[17] S. E. Skipetrov and I. M. Sokolov, Absence of anderson localization of light in a random ensemble of point scatterers, Phys. Rev. Lett. **112**, 1 (2014).
[18] L. Bellando, A. Gero, E. Akkermans, and R. Kaiser, Cooperative effects and disorder: A scaling analysis of the spectrum of the effective atomic Hamiltonian, Phys. Rev. A. **90**, 1 (2014).
[19] R. R. Naraghi and A. Dogariu, Phase transitions in diffusion of light, Phys. Rev. Lett. **117**, 1 (2016).
[20] N. Cherroret, D. Delande, and B. A. Van Tiggelen, Induced dipole-dipole interactions in light diffusion from point dipoles, Phys. Rev. A **94**, 1 (2016).
[21] D. S. Wiersma, P. Bartolini, A. Lagendijk, and R. Righini, Localization of light in a disordered medium, Nature **390**, 671 (1997).
[22] F. Scheffold, R. Lenke, R. Tweer, and G. Maret, Localization or classical diffusion of light?, Nature **398**, 206 (1999).
[23] R. L. Weaver and O. I. Lobkis, Ultrasonics without a

source: thermal fluctuation correlations at MHz frequencies, Phys. Rev. Lett. **87**, 134301 (2001).
[24] A. Derode, E. Larose, M. Campillo, and M. Fink, How to estimate the Green's function of a heterogeneous medium between two passive sensors? Application to acoustic waves, Appl. Phys. Lett. **83**, 3054 (2003).
[25] M. Campillo and A. Paul, Long-Range Correlations in the Diffuse Seismic Coda, Science **299**, 547 (2003).
[26] E. Larose, L. Margerin, A. Derode, B. A. van Tiggelen, M. Campillo, N. Shapiro, A. Paul, L. Stehly, and M. Tanter, "Correlation of random wave- fields: an interdisciplinary review, Geophysics **71**, SI11 (2006).
[27] A. Badon, G. Lerosey, C. Boccara, M. Fink, and A. Aubry, Retrieving Time-Dependent Green's Functions in Optics with Low-Coherence Interferometry, Phys. Rev. Lett. **114**, 023901 (2015).
[28] A. Badon, D. Li, G. Lerosey, A. C. Boccara, M. Fink, and A. Aubry, Spatio-Temporal Imaging of Light Transport in Highly Scattering Media under White Light Illumination, Optica **3**, 11 (2016).
[29] P.-E. Wolf and G. Maret, Weak localization and coherent backscattering of photons in disordered media, Phys. Rev. Lett. **55**, 2696 (1985).
[30] M. P. V. Albada and A. Lagendijk, Observation of weak localization of light in a random medium, Phys. Rev. Lett. **55**, 2692 (1985).
[31] D. S. Wiersma, M. P. van Albada, B. A. van Tiggelen, and A. Lagendijk, Experimental Evidence for Recurrent Multiple Scattering Events of Light in Disordered Media, Phys. Rev. Lett. **74**, 4193 (1995).
[32] A. Aubry, L. A. Cobus, S. E. Skipetrov, B. A. van Tiggelen, A. Derode, and J. H. Page, Recurrent scattering and memory effect at the anderson localization transition, Phys. Rev. Lett. **112**, 043903 (2014).
[33] E. Abrahams, P. W. Anderson, D. C. Licciardello, and T. V. Ramakrishnan, Scaling theory of localization: Absence of quantum diffusion in two dimensions, Phys. Rev. Lett. **42**, 673 (1979).
[34] M. S. Patterson, B. Chance, and B. C. Wilson, Time resolved reflectance and transmittance for the noninvasive measurement of tissue optical properties, Appl. Opt. **28**, 2331 (1989).
[35] M. Störzer, *Anderson Localization of Light*, Ph.D. thesis, Universität Konstanz (2006).
[36] W. Bührer, *Anderson Localization of Light in the Presence of Non-linear Effects*, Ph.D. thesis, Universität Konstanz (2012).
[37] T. Sperling, *The experimental search for Anderson localisation of light in three-dimensions*, Ph.D. thesis, Universität Konstanz (2015).
[38] L. Schertel, I. Wimmer, B. P., C. M. Aegerter, G. Maret, S. Polarz, and G. J. Aubry, Tunable high-index photonic glasses, Phys. Rev. M **3**, 015203 (2019).
[39] See Supplemental Material at ... for further details.
[40] T. Sperling, W. Bührer, C. M. Aegerter, and G. Maret, Direct determination of the transition to localization of light in three dimensions, Nat. Photonics **7**, 48 (2013).
[41] J. H. Page, H. P. Schriemer, A. E. Bailey, and D. A. Weitz, Experimental test of the diffusion approximation for multiply scattered sound, Phys. Rev. E **52**, 3106 (1995).
[42] A. Aubry and A. Derode, Ultrasonic imaging of highly scattering media from local measurements of the diffusion constant: Separation of coherent and incoherent intensities, Phys. Rev. E **75**, 026602 (2007).
[43] N. Cherroret, S. E. Skipetrov, and B. A. van Tiggelen, Transverse confinement of waves in three-dimensional random media, Phys. Rev. E. **82** (2010).
[44] R. Vreeker, M. P. van Albada, R. Sprik, and A. Lagendijk, Femtosecond time-resolved measurements of weak localization of light, Phys. Lett. A **132**, 51 (1988).
[45] A. Tourin, A. Derode, P. Roux, B. A. van Tiggelen, and M. Fink, Time-dependent coherent backscattering of acoustic waves, Physical Review Letters **79**, 3637 (1997).
[46] A. Aubry, A. Derode, P. Roux, and A. Tourin, Coherent backscattering and far-field beamforming in acoustics, The Journal of the Acoustical Society of America **121**, 70 (2007).
[47] L. Margerin, M. Campillo, and B. A. van Tiggelen, Coherent backscattering of acoustic waves in the near field, Geophys. J. Int. **145**, 593 (2001).
[48] B. A. van Tiggelen, L. Margerin, and M. Campillo, Coherent backscattering of elastic waves: Specific role of source, polarization, and near field, J. Acoust. Soc. Am. **110**, 1291 (2001).
[49] D. Vollhardt and P. Wölfle, Scaling equations from a self-consistent theory of Anderson localization, Phys. Rev. Lett. **48**, 699 (1982).
[50] S. E. Skipetrov and B. A. van Tiggelen, Dynamics of Anderson localization in open 3D media, Phys. Rev. Lett. **96**, 043902 (2006), 0508726v2.
[51] K. M. Douglass, S. John, T. Suezaki, G. A. Ozin, and A. Dogariu, Anomalous flow of light near a photonic crystal pseudo-gap, Opt. Express **19**, 25320 (2011).
[52] The temporal scaling laws of the return probability differ from the ones considered in a previous acoustics work [32]. While the previous study considered the far-field reflectance of the medium, *i.e* an energy flux density [34], here we probe the energy density at the sample surface.
[53] C. W. J. Beenakker, Random-matrix theory of quantum transport, Rev. Mod. Phys. **69**, 731 (1997).
[54] B. Gérardin, J. Laurent, A. Derode, C. Prada, and A. Aubry, Full transmission and reflection of waves propagating through a maze of disorder, Phys. Rev. Lett. **113**, 173901 (2014).
[55] J. W. Goodman, *Introduction to Fourier Optics* (Mc Graw Hill, New York, 1996).
[56] R. L. Weaver and O. I. Lobkis, Diffuse fields in open systems and the emergence of the green's function (L), J. Acoust. Soc. Am. **116**, 2731 (2004).
[57] E. Akkermans and G. Montambaux, *Mesoscopic Physics of Electrons and Photons* (Cambridge University Press, Cambridge, 2007).
[58] V. Barolle, J. Scholler, P. Mecê, J.-M. Chassot, K. Groux, M. Fink, A. C. Boccara, and A. Aubry, Manifestation of aberrations in full-field optical coherence tomography, Opt. Express **29**, 22044 (2021).
[59] P. R. Bevington and D. K. Robinson, *Data Reduction and Error Analysis for the Physical Sciences*, 2nd ed. (McGraw-Hill, New York, 1992).